ELSEVIER

Contents lists available at ScienceDirect

Composites Science and Technology

journal homepage: http://www.elsevier.com/locate/compscitech





Laser induced graphene for in-situ ballistic impact damage and delamination detection in aramid fiber reinforced composites

Kelsey Steinke^a, LoriAnne Groo^b, Henry A. Sodano^{a,b,c,*}

- a Department of Materials Science and Engineering, University of Michigan, Ann Arbor, MI 48109, United States
- b Department of Aerospace Engineering, University of Michigan, Ann Arbor, MI 48109, United States
- ^c Department of Macromolecular Science and Engineering, University of Michigan, Ann Arbor, MI 48109, United States

ARTICLE INFO

Keywords: Multifunctional composites Laser-induced graphene Sensing Impact behavior Delamination

ABSTRACT

Aramid fiber reinforced polymer composites have been shown to exhibit impressive mechanical properties, including high strength-to-weight ratio, excellent abrasion resistance, and exceptional ballistic performance. For these reasons, aramid composites have been heavily used in high impact loading environments where ballistic properties are vital. In-situ damage monitoring of aramid composites under dynamic loading conditions typically requires externally bonded sensors, which add bulk and are limited by size and space constraints. To overcome these limitations, this work presents a piezoresistive laser induced graphene (LIG) interface for embedded impact sensing in aramid fiber reinforced composites. Through the monitoring of electrical impedance during ballistic impact, information regarding time and severity of the impact is obtained. The impact velocity correlates with the impedance change of the composites, due to delamination between aramid plies and damage to the LIG interface. The delamination length in Mode I specimens also correlates to changes in electrical impedance of the composite. The interlaminar fracture toughness and areal-density-specific V_{50} of the LIG aramid composites increased relative to untreated aramid composites. This work demonstrates a methodology to form multifunctional aramid-based composites with a LIG interface that provides both improved toughness and imbedded sensing of impact and damage severity during ballistic impact.

1. Introduction

Aramid fibers have played an integral role in the production of high performance composites for a wide variety of structural applications including sporting goods, helicopter blades, maritime vessels, and especially ballistic applications such as helmets, combat shields, and armored vehicles [1,2]. The use of aramid composites in these applications is due to their superior properties such as a high strength to weight ratio, abrasion and impact resistance, and high energy absorption [3]. Nonetheless, aramid fiber reinforced composites are prone to significant structural and ballistic damage due to harsh operating environments, thus risking catastrophic failure in the employed structure. Therefore, the ability to detect such damage can help assess the health of the structure, monitor its state, and most importantly avoid catastrophic failure by detecting damage while in its early stages. While damage detection can be achieved in conductive fiber reinforced composites, such as carbon, using their innate piezoresistivity to correlate changes in impedance to generated damage, this remains a challenge in aramid

composites due to their electrically insulating nature. Thus, it is necessary to develop new techniques capable of monitoring damage in aramid fiber reinforced composites to improve their safety and reliability.

Multiple studies have focused on post-service damage assessment in aramid fiber reinforced polymer composites, using methods which include ultrasonic air C-scan [4], micro computerized tomography [5], and laser Raman microprobe [6]. While these methods are capable of successfully detecting impact damage in aramid composites, all require the removal of the impacted area of the composite from the structure combined with additional sample preparation prior to employ the damage detection technique. To overcome the need to remove the composite from service for damage assessment, researchers have developed methods using integrated sensors. Zivkovic et al. demonstrated in-situ damage sensing in aramid fiber reinforced laminates by monitoring changes in optical signals through embedded fiber optic sensors [7]. However, integration of the fiber optic sensors within the composite requires extensive sample preparation and can produce a defect which reduces material strength. Another technique was

^{*} Corresponding author. Department of Materials Science and Engineering, University of Michigan, Ann Arbor, MI 48109, United States. E-mail address: hsodano@umich.edu (H.A. Sodano).

proposed by Rosa et al., where embedded polyvinylidene fluoride (PVDF) acoustic emission sensors were used for in-situ damage detection in aramid fiber reinforced composites [8]. Additionally, Groo et al. demonstrated the use of hydrothermally grown zinc oxide nanowires on aramid fibers with carbon fiber electrodes to detect multiple modes of damage by passively monitoring the voltage emission across a composite [9]. However, these methods typically require more intensive sample preparation to incorporate damage detection which presents challenges in manufacturing and scale up for industrial use.

Researchers have monitored in-situ damage in fiber reinforced polymer composites using a wide variety of methodologies such as through optical fibers [10,11], acoustic emission testing [12,13], and resistance-based sensing [14,15]. Resistance-based structural health monitoring has been extensively investigated by several researchers for carbon and glass fiber reinforced composites. Early approaches to in-situ damage sensing of carbon fiber reinforced polymer composites took advantage of the inherent piezoresistivity of carbon fibers by monitoring the electrical resistance of the fibers during loading [16-19]. This is commonly achieved using the four-probe resistance monitoring technique where a DC current is applied through the area under investigation while the resultant voltage across the same area is monitored. The impedance can then be calculated using Ohm's law. As damage, such as fiber fracture or delamination, occurs within the carbon fiber-based composite, the conductive pathways along the fiber are disrupted resulting in a measurable increase in the electrical impedance [16–19]. Moreover, different modes of damage are distinguishable by changing the direction of the resistance measurements, as fiber breakage is more detectable using measurements along the fiber axis, whereas the detection of delamination is enhanced when performing measurements through the thickness of the composite [19]. However, such damage sensing approaches are limited to composites containing conductive fiber reinforcement, such as carbon. To overcome this limitation, researchers have investigated carbon-based nanofillers, such as carbon black [14], graphene nanoparticles [20] and sheets [21], carbon nanotubes (CNTs) [14,15,22-24], and CNT paste [25] as means to introduce conductivity into traditionally insulating fiber reinforced composites. For example, Alexopoulos et al. showed that adding CNT-based fibers between glass fabric plies adds piezoresistivity to an otherwise insulating composite [23]. The resultant modified glass fiber reinforced composites were shown to exhibit a direct correlation between the electrical impedance and the applied tensile strain without any degradation of the mechanical performance when compared to the untreated composite [23]. However, CNTs present dispersion challenges due to their tendency to agglomerate as a result of van der Waals interaction, leading to non-uniform piezoresistivity and less than theoretical mechanical performance [26,27]. Sanchez et al. dispersed doped graphene nanoparticles within the uncured matrix of glass fiber reinforced composites, which introduced conductive networks to detect deformation and damage [20]. The reported results conclusively show a correlation between the resistance of the specimen and the crack length during Mode I and Mode II interlaminar fracture toughness testing [20]. However, despite the widespread research on resistance-based sensing for carbon and glass fiber reinforced polymer composites, similar efforts are lacking for aramid fiber reinforced polymer composites.

Laser induced graphene (LIG) has recently gained research traction due to the ease of production and inherent piezoresistivity [28]. The graphitic structure is obtained through the conversion of $\rm sp^3$ -carbon atoms in polyimide to $\rm sp^2$ -carbon using a commercial $\rm CO_2$ infrared laser in an ambient environment, which results in a highly conductive, flexible surface with excellent thermal and electrical properties [28]. Since its initial discovery, the potential applications of LIG have expanded to include joule heating [29], resistive memory devices [29], biomedical applications [30,31], flexible sensors [32,33], and composite strain sensors [29,34–36]. Additionally, although LIG is most commonly generated from polyimide films, Chyan et al. demonstrated that LIG could be directly formed on a wide variety of polymeric and

non-polymeric surfaces, including aramid fibers [30]. Recently, Nasser et al. reported that LIG-coated aramid fiber reinforced polymer matrix composites exhibited improved short beam and Mode I interlaminar fracture toughness due to an increased interlocking mechanism and chemical interaction in the interlaminar region [37]. Therefore, the combination of the piezoresistive properties of LIG and the ease of application with aramid fabrics presents a material with promising potential with regards to in-situ and resistance-based damage detection for aramid fiber reinforced composites. This application of LIG was recently investigated by Groo et al. who utilized LIG-coated aramid fabric as the reinforcement for self-sensing fiber reinforced composites [36]. The modified aramid-based composites were shown to be capable of tracking both tensile and flexural strain in addition to detecting tensile damage in situ. However, up to this point, the ballistic impact performance and sensing capabilities of the LIG-coated aramid fabrics is yet to be investigated despite the traditional ballistic applications of aramid-based composites.

The work presented here investigates the potential of LIG for in-situ impact damage and delamination detection in aramid fiber reinforced polymer composites. To accomplish this, the LIG was directly formed on the aramid fabric using a laser printer, before infusing the treated fabric to form aramid laminates. The ability of the LIG to sense ballistic damage was evaluated through impacting the treated aramid laminates using a gas gun, and the electrical impedance was simultaneously monitored using the four-point probe technique. A correlation between the velocity of the projectile and the change in specimen impedance was established by impacting multiple samples over a range of projectile velocities. Additionally, resistance measurements taken during Mode I interlaminar fracture tests were used to investigate the correlation between the change in resistance and delamination between composite plies. Concurrently, the impact limit and Mode I fracture toughness were assessed to ensure that the LIG process on the aramid fiber does not detract from the structural and ballistic performance of the laminates. The result is thus a multifunctional structural material with embedded self-sensing capabilities.

2. Experimental section

2.1. Laser induced graphene process on aramid fiber and characterization

LIG was generated on the surface of the aramid fabric using the method described by Nasser et al. [37]. Prior to the laser treatment, the aramid fabric (Kevlar® KM2+ fabric plain-weave, style 790, scoured CS-800, received from BGF Industries) was successively sonicated in acetone and ethanol for 10 min to remove organic surface contaminants, and then dried in a vacuum oven at 100 °C for 1 h. The carbonization of only one side of the aramid fabric was performed using a 40W CO $_2$ laser printer (Epilog Zing 16) operated in raster mode, at a speed of 1 cm 2 s $^{-1}$, pulsing density of 400 dots per inch (DPI), and output power of 20% (Fig. 1A). The parameters used in this work have previously been found to maintain the specific strength of the fabric [37]. Following the laser treatment, the morphology of the LIG-treated aramid fabric surface was characterized using a JEOL JSM-7800FLV field-emission scanning electron microscope (SEM).

2.2. Gas gun impact specimen fabrication

After LIG was generated on the aramid fabric surface (Fig. 1A), three 3 by 3-inch plies of aramid fabric were combined into a laminate using vacuum assisted resin transfer molding (VARTM) as shown in Fig. 1B. Epon 862 and Curing Agent W (100:26.4) resin was used as the matrix, and the laminates were cured under vacuum at 100 psi and 177 °C for 3 h in a hot press. After the laminate is fabricated, to enable electrical impedance measurements during ballistic testing using the four-point probe method, two silver paint rings were added to each side of the LIG-treated composites as seen in Fig. 2A and B and 33-gauge copper

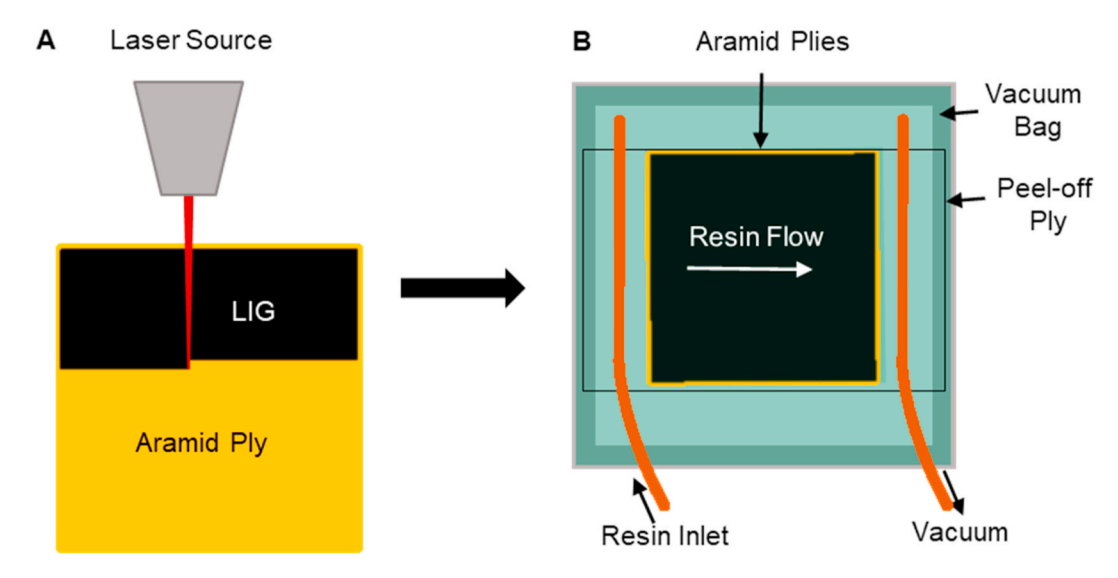


Fig. 1. Flow chart schematic of A) the LIG generation on aramid fabric to the B) vacuum assisted resin transfer molding of the LIG-treated aramid laminate.

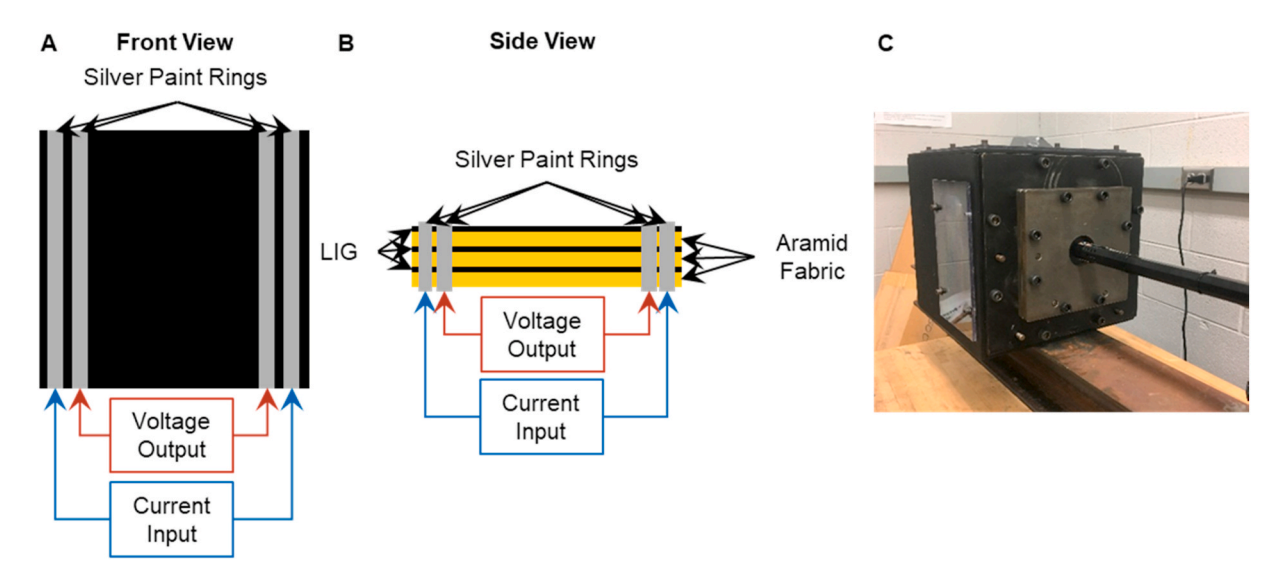


Fig. 2. A) Front view schematic of four-point probe resistance monitoring adopted on an aramid composite with LIG. B) Side view schematic of four-point probe resistance monitoring adopted on an aramid composite with LIG. C) Image of ballistic setup.

wires were attached to the surface of each silver paint ring using additional silver paint and electrical tape.

2.3. Gas gun impact testing

Following sample preparation, the composite laminates were impacted using a customized gas gun, the details of which are fully described by Stenzler et al. [38]. The samples were placed between two steel plates with a 2.5-inch diameter target region to constrain any undesired motion of the laminate during testing. Once the composite was securely fixed, the barrel of the gas gun was placed 0.25 inches away from the center of the composite (Fig. 2C). The projectile, comprised of 4130 alloy steel with a mass of 29 g and an 11.4 diameter hemispherical face, was propelled down the barrel by releasing a predetermined set gas pressure. Two photogates, placed 19.5 mm apart at the end of the barrel, were used to measure the amount of time needed for the projectile to pass between them, thus allowing for the calculation of the projectile velocity at the point of impact. To quantify the ballistic performance of each sample set, the $\rm V_{50}$ is considered as the figure of merit. The $\rm V_{50}$ ballistic limit is calculated by averaging the three lowest speeds at which

the bullet did penetrate and the three highest speeds at which the bullet did not penetrate the composite specimen. During ballistic testing, the copper wires attached to the outermost silver paint rings were used to apply 4 mA direct current through the sample using a BK Precision® model 9130 triple output programmable DC power supply, while the voltage was simultaneously measured across the copper wires attached to the two innermost silver paint rings using a National Instruments 4431 data acquisition system (DAQ). For clarity, a schematic of the four-point probe resistance monitoring schematic can be seen in Fig. 2A and 2B.

2.4. Mode I specimen fabrication

The Mode I interlaminar fracture toughness of the LIG-treated aramid fiber reinforced composites was assessed as recommended per ASTM D5528-13. Specifically, each laminate was fabricated by VARTM (Fig. 1B) and consisted of 16 plies of aramid fabric with an EPON 862/Curing Agent W resin system. In order to form a pre-crack within the laminate, a 50 mm Teflon sheet was inserted between the two center plies. It should be noted that in order to enable in-situ resistance

measurements, the two center plies were treated with LIG (Fig. 1A), and the LIG interfaces were placed facing each other (Fig. 3A). The composite plate was then cut using a diamond saw to specimens which were 14 cm long, 23 mm wide, and 3 mm thick. Loading hinges were attached to the outer surfaces of each sample using a high shear strength epoxy (Loctite® 9430 $^{\text{TM}}$ Hysol®) which was cured in an oven at 83 °C for 1 h.

2.5. Mode I fracture toughness testing

The completed samples were tested using an Instron model 5982 load frame with a 100 kN load cell at a crosshead extension rate of 2 mm/min. After the crack was allowed to propagate to the length of the Teflon pre-crack, the Teflon insert was removed and copper wires were attached to each LIG surface using silver paint and electrical tape. Throughout the duration of the test, the electrical impedance between the two copper wires, and thus the two LIG plies, was measured as the delamination extended along the length of the specimen using a Wheatstone bridge with a constant voltage input provided by a Hewlett Packard model 6217A DC power supply. A schematic of the resistance monitoring method is shown in Fig. 3A.

3. Results and discussion

3.1. LIG characterization

To integrate a piezoresistive sensing element within traditionally insulating aramid fiber composites, one surface of each aramid fabric ply was coated with conductive LIG. Notably, no pre- or post-treatment of the aramid fibers was required prior to the conversion of the surface fibers to LIG. Following the laser treatment, the surface morphology of the LIG-coated aramid fabric was investigated using SEM imaging. As seen in Fig. 4B, the exposed surface fibers of the woven aramid fabric are drastically changed following the laser treatment, relative to an untreated aramid fiber (Fig. 4A). Rather than displaying the smooth surface of untreated aramid fibers, the surface of the laser treated fibers possess a three-dimensional (3D) microporous fibrous structure. Previous studies have investigated the effect of the laser output power, pulsing density, and focusing density on the resultant LIG microstructure on the aramid surface and the corresponding mechanical properties [30, 37]. Here, a pulse density of 400 DPI, defocusing distance of 0.3 mm, and output power of 20% were chosen to generate a uniform coating on the surface of the exposed aramid fibers [37]. According to Fig. 4C, the thickness of the aramid fabric is \sim 400 μm and the LIG layer is measured to be ${\sim}25~\mu\text{m}$, which is equivalent to the diameters of 2 individual aramid fibers. It should be noted that the laser induction parameters used in this work result in the complete conversion of the top aramid surface to a textured graphitic layer, while simultaneously limiting the laser penetration depth, thus leaving the majority of the aramid fibers intact and preserving the specific strength of the fabric as shown in

Fig. 4C [37]. The converted amorphous carbon atoms create a continuous conductive top surface; however, the untreated portion of the fabric remains insulating through its thickness, which confirms that the LIG remains on the surface and does not completely penetrate the fabric. The fibrous structure of the LIG coating has previously been shown to result in improved mechanical interlocking and increased surface area interaction between the reinforcing fibers and the matrix, therefore strengthening the interlaminar region in the aramid laminate. The porous nature of LIG also permits for easy infusion and resin wetting during the VARTM fabrication process. Furthermore, a small portion of the LIG remains exposed at the surface of the laminate, which allows for direct contact between the LIG and the measurement probes without the need to remove any of the matrix at the surface. The final resistance values of the ballistic composites ranged between \sim 40 and 100 Ω measured using the four-point probe method. In order to monitor the average resistance of the entire composite during ballistic impact, the silver paint rings shown in Fig. 1A and 1B were designed to connect the three plies of the composite around the perimeter. Thus, the final measured resistance values represent an average value for the entire composite specimen.

3.2. Gas gun ballistic impact testing

The V₅₀ ballistic limit or the ballistic performance of a composite can assist in both understanding the limits of the material for specific applications and aiding in the prediction of the extent of damage experienced by the composite based on the ballistic impact velocity. Here, the V₅₀ of the LIG-treated aramid fiber composites is compared to untreated aramid fiber composites to ensure that the LIG treatment does not negatively affect the ballistic performance of the composites. A total of 12 untreated samples and 12 LIG-treated samples were prepared, of which at least 5 samples were penetrated by the projectile and at least 5 samples successfully stopped the projectile from penetrating. In order to qualify as penetrating the composite, 100% of the projectile was required to pass through the composite and impact the clay trap located 2 inches behind the composite. The projectile velocities for each sample set along with the penetration status and the resulting V₅₀ values for untreated and LIG-treated samples are shown in Table 1. It can be noted that the larger range in impact speed for the LIG-treated composites was used to collect a wider and more complete range of data points as the authors investigated a relationship between the impact velocity and percent change in resistance, as seen Fig. 4B. For this reason, more impact speeds are reported for LIG-treated aramid composites relative to the untreated composites (Table 1). With regards to ballistic limit, the 6 speeds used to calculate the V₅₀ for the untreated samples ranged between 22.1 m/s to 26.6 m/s for a span of 4.5 m/s, while the LIG-treated samples ranged between 19.1 m/s and 23.5 m/s for a range of 4.4 m/s. Therefore, the V₅₀ for both the untreated and LIG-treated samples were obtained over a similar range, thus allowing for an accurate comparison

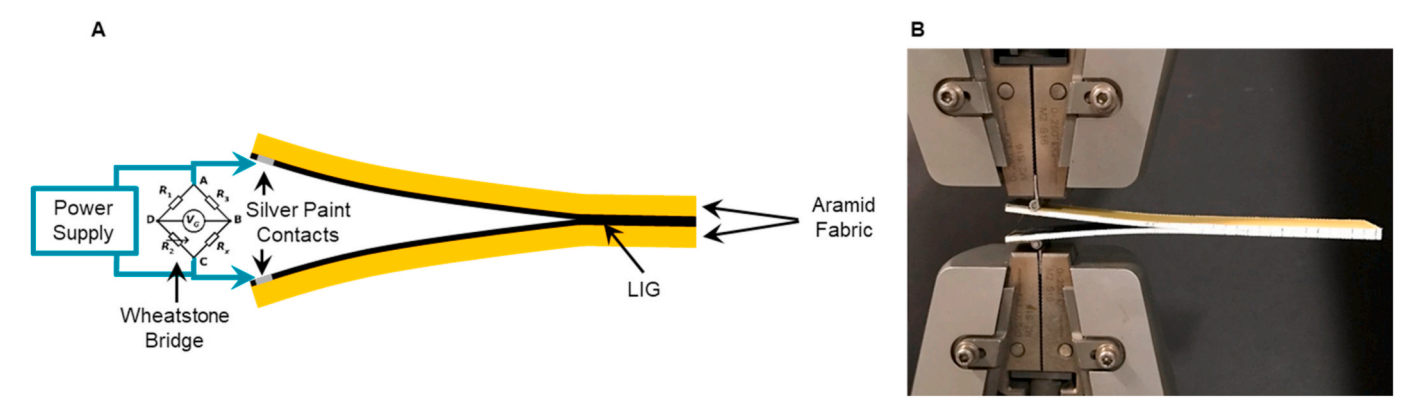


Fig. 3. A) Schematic of resistance monitoring method with increasing crack length during Mode I testing. B) Mode I interlaminar fracture toughness setup.

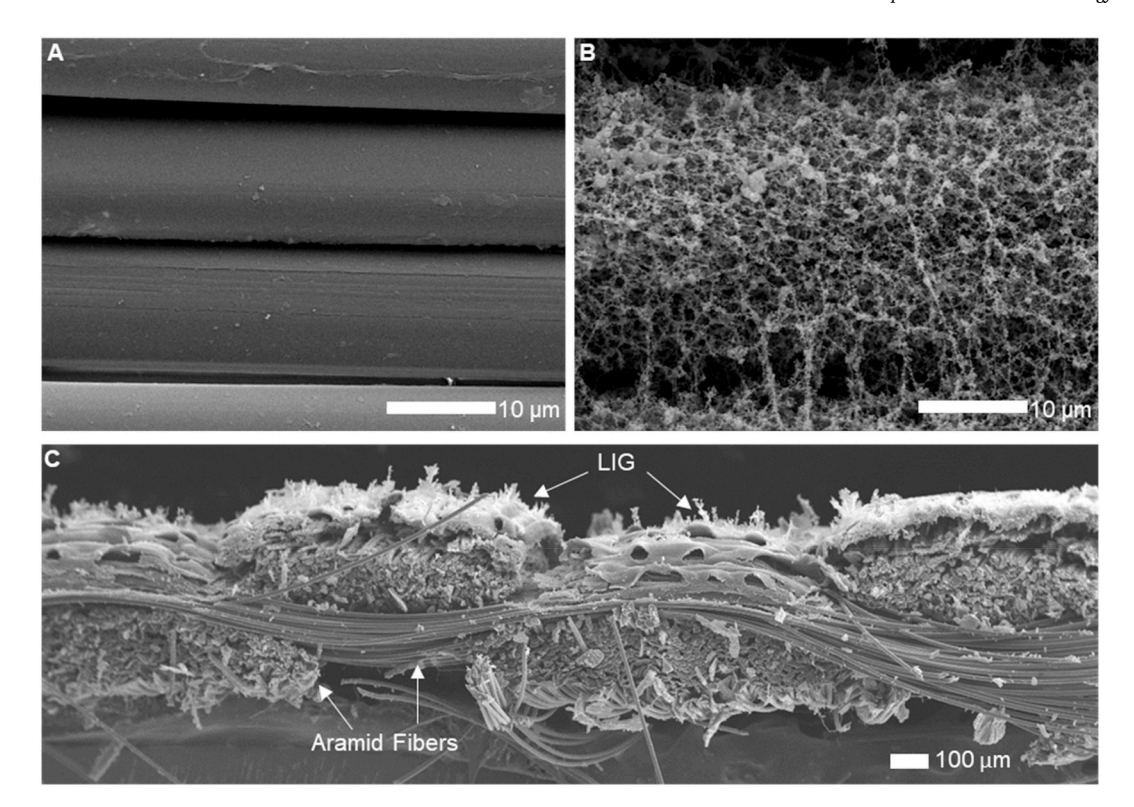


Fig. 4. SEM image of A) untreated aramid fibers, and B) LIG microstructure on aramid fiber. C) LIG conversion of the top aramid fibers with the rest of the aramid fibers within the fabric intact.

 $\label{eq:table 1} \textbf{Table 1} \\ \textbf{Projectile speed and penetration status of each ballistic test used to calculate the} \\ \textbf{V}_{50} \ \ \text{of untreated and LIG-treated aramid fiber reinforced composites.} \\ \\ \textbf{Table 1} \\ \textbf{V}_{50} \ \ \text{of untreated and LIG-treated aramid fiber reinforced composites.} \\ \\ \textbf{V}_{50} \ \ \text{of untreated and LIG-treated aramid fiber reinforced composites.} \\ \textbf{V}_{50} \ \ \text{of untreated and LIG-treated aramid fiber reinforced composites.} \\ \textbf{V}_{50} \ \ \text{of untreated and LIG-treated aramid fiber reinforced composites.} \\ \textbf{V}_{50} \ \ \text{of untreated and LIG-treated aramid fiber reinforced composites.} \\ \textbf{V}_{50} \ \ \text{of untreated and LIG-treated aramid fiber reinforced composites.} \\ \textbf{V}_{50} \ \ \text{of untreated and LIG-treated aramid fiber reinforced composites.} \\ \textbf{V}_{50} \ \ \text{of untreated and LIG-treated aramid fiber reinforced composites.} \\ \textbf{V}_{50} \ \ \text{of untreated and LIG-treated aramid fiber reinforced composites.} \\ \textbf{V}_{50} \ \ \text{of untreated aramid fiber reinforced composites.} \\ \textbf{V}_{50} \ \ \text{of untreated aramid fiber reinforced composites.} \\ \textbf{V}_{50} \ \ \text{of untreated aramid fiber reinforced composites.} \\ \textbf{V}_{50} \ \ \text{of untreated aramid fiber reinforced composites.} \\ \textbf{V}_{50} \ \ \text{of untreated aramid fiber reinforced composites.} \\ \textbf{V}_{50} \ \ \text{of untreated aramid fiber reinforced composites.} \\ \textbf{V}_{50} \ \ \text{of untreated aramid fiber reinforced composites.} \\ \textbf{V}_{50} \ \ \text{of untreated aramid fiber reinforced composites.} \\ \textbf{V}_{50} \ \ \text{of untreated composite composites.} \\ \textbf{V}_{50} \ \ \text{of untreated composite composites.} \\ \textbf{V}_{50} \ \ \text{of untreated composite comp$

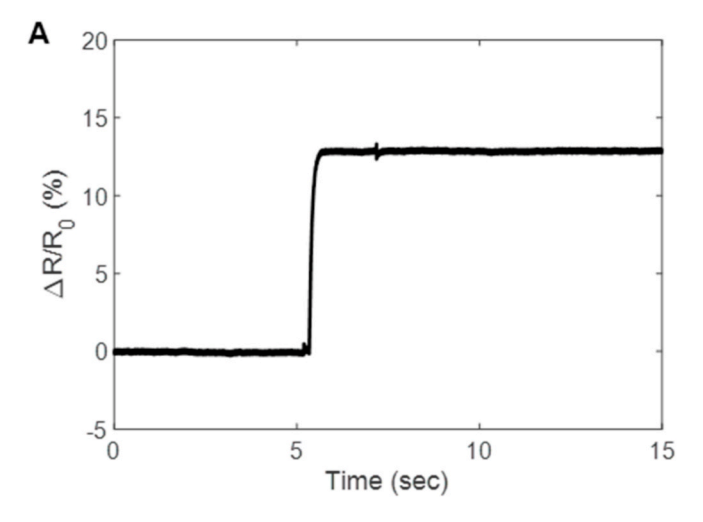
Untreated Aramid Composite		LIG-Treated Aramid Composite	
Impact Speed (m/s)	Penetration	Impact Speed (m/s)	Penetration
18.2	No	6.9	No
20.2	No	10	No
21	No	19.1	No
22.1	No	20	No
23.4	No	21.3	Yes
25.4	No	23	No
25.6	Yes	23.1	Yes
26	Yes	23.5	Yes
26.6	Yes	25	Yes
28.2	Yes	26	Yes
29.8	Yes	38	Yes
30.5	Yes	48	Yes
		81.62	Yes
$V_{50} = 24.6 \ m/s$		$V_{50} = 21.7 \ m/s$	

of their ballistic limit.

Although a knowledge of the ballistic limit of LIG-treated aramid composites is important for the prediction of the amount of damage experienced by the composite, a direct comparison between the V_{50} of the untreated and LIG-coated aramid composites does not provide an accurate representation of the relative ballistic performance of each sample set. The weight of the aramid fabric is reduced during the irradiation process as the exterior fibers, which are exposed to the laser, are converted to a porous graphene interface, thus resulting in lower aerial density aramid composites. Given that the areal density of a fabric is important to the ballistic performance, the areal-density-specific V_{50} presents a more reliable parameter for comparison. Therefore, for accuracy, the areal-density-specific V_{50} was calculated for each sample set by dividing the raw V_{50} value by the respective areal density. Specifically, the weight of three untreated and three LIG-treated plies were

measured and divided by the area of the sample (7.62 cm x 7.62 cm), resulting in areal-densities of 0.073 g/cm² for the untreated aramid fabric plies, and 0.062 g/cm² for the LIG-treated plies. When normalized, the areal-density-specific V_{50} is found to be 0.033 $m^3/s/g$ and 0.035 $m^3/s/g$ for the untreated and LIG-treated fabric, respectively. Based on the normalized V_{50} , the ballistic performance of the LIG-treated composite is improved relative to that of the untreated aramid composite. This can be attributed to the increased friction between the LIG-treated aramid fabric surface and the surrounding matrix, as the LIG provides an interlocking mechanism and increases surface area interactions. Therefore, the ability of the projectile to penetrate the composite is reduced, and the ballistic energy absorption performance of the aramid laminates is increased.

To analyze the ability of the integrated piezoresistive LIG interface to detect ballistic damage in-situ, the electrical impedance of the LIGtreated aramid specimens was measured using the four-point probe resistance monitoring method throughout the duration of each ballistic test. Fig. 5A shows the percent change in the electrical impedance of one representative sample during projectile impact. As seen in Fig. 5A, once the LIG coated specimen is impacted, an immediate increase in electrical impedance is observed. This increase is attributed to the rapid physical separation between conductive carbon-carbon contacts within each LIG surface resulting from fiber fracture caused by the projectile, combined with inter-ply delamination as a result of the projectile impact creating air and physical separation between the aramid plies thus further damaging the LIG interfaces. It should be noted that the noise observed at approximately 7 s in Fig. 5A is attributed to the pressure valve closing after releasing the gas pressure to push the projectile down the barrel towards the sample. When the valve closes, it releases an extra burst of gas which travels down the barrel and vibrates the sample, causing a small temporary change in resistance. This noise was observed in all samples and can be seen again in Fig. 6E at varying impact speeds. As a result, it is intuitive to assume that higher projectile velocities will generate a larger extent of damage to the aramid laminates, where a greater increase in electrical impedance is expected. To investigate this



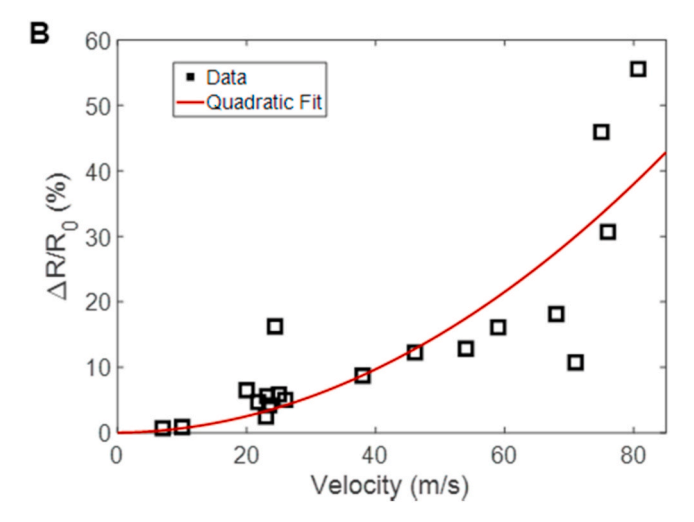


Fig. 5. A) Representative change in impedance of one ballistic impact sample. B) Change in impedance percent change vs. velocity of impact for LIG-treated aramid fiber composites.

relationship, varying projectile velocities were tested and the correlation between the percent change in impedance and the projectile velocity was evaluated (Fig. 5B). The velocity is increased from approximately 7 m/s to 81 m/s and the corresponding change in electrical impedance increased from less than 1% to over 55%. As the velocity is increased, the amount of damage and change in impedance are also increased as the laminate absorbs some portion of the impact energy resulting in significant fiber fracture and delamination. A quadratic fit was applied to the impedance percent change vs impact velocity (Fig. 5B) and with a nonlinear least squares regression analysis, the quadratic fit predicts the trend of the impedance percent change and velocity with a coefficient of determination (R²) value of 0.72. The relationship between the velocity and the percent change in impedance thus follows a quadratic trend through the range investigated which is attributed to the similarly quadratic relationship between velocity and kinetic energy. Therefore, it is assumed that the energy absorbed by the composite is loosely related to the kinetic energy of the projectile. Although additional factors such as friction are expected to have an effect, this assumption allows for the approximate prediction of the velocity using the percent change in impedance.

To further investigate the method of energy absorption and thus gain greater understanding of the previously observed trend between electrical impedance change and ballistic impact velocity, the impacted laminates were visually examined and compared. Through macroscopic visual inspection, it can be seen that the plies comprising each laminate delaminated during impact, thus.

Introducing air pockets between the plies. This delamination is expected to further damage the LIG, thus increasing the electrical impedance of the sample. Moreover, from visual inspection it can be seen that inter-ply delamination is more prominent with increasing projectile velocity, reducing carbon-carbon contact area in each LIG layer, resulting in a larger percent increase in the electrical impedance of the sample. For reference, Fig. 6 shows four representative samples which are damaged with increasing impact velocities (Fig. 6A-G) and their corresponding percent change in impedance (Fig. 6I). As the velocity increases, the delaminated area, which is visible as the lighter portion of the composite from the top surface, approximated by dashed black contours, and the laminates cross section, is observed to grow larger. Additionally, the fibers surrounding the impact hole in the composite, resulting from the penetration of the projectile, also show increased damage in the form of fiber failure. Therefore, the increase in impedance is dictated by the size of the damage due to penetration in addition to the delamination area which are both seen to increase with increasing impact velocities.

3.3. Mode I interlaminar fracture toughness testing

Since the interlaminar region of composites are typically prone to failure, it is important that the Mode I interlaminar fracture toughness of the composite is not compromised due to the addition of LIG to the interlaminar region. At least 5 samples of both untreated aramid composites and LIG-treated aramid composites were tested to calculate the Mode I interlaminar fracture toughness. Fig. 7 shows the average fracture toughness (Fig. 7A) and a representative fracture toughness vs extension curves (Fig. 7B) for an untreated and a LIG-treated sample. As seen in Fig. 7, the interlaminar fracture toughness of the untreated aramid composite was 437 J/m^2 , and the LIG-treated composites exhibited an increased interlaminar fracture toughness at 476 J/m^2 .

The improved fracture toughness can be attributed to an interlocking mechanism from the fibrous LIG microstructure mechanically bridging the gap between adjacent plies, and therefore requiring more energy to drive crack propagation in the double cantilever beams. A similar mechanism has been previously reported in the literature, and is often termed as "nanostitching" [37,39,40]. The fracture surfaces of the LIG-treated aramid Mode I samples were imaged and shown in Fig. 8. While stick slip behavior can be seen in Fig. 8A, the interlaminar failure mode is a cohesive one, allowing the LIG-aramid fiber composites to withstand higher loads as the crack propagates within the interlaminar region. Fig. 8C and D demonstrate this strong adhesion between the LIG and epoxy resin as there is a substantial amount of epoxy blocks remaining on the fracture surface. These findings are in agreement with other studies that report cohesive failure in LIG coated aramid fiber Mode I interlaminar fracture toughness samples [37]. Thus, the added LIG interface improves the fracture toughness of the aramid fiber reinforced composites in addition to contributing piezoresistance.

In addition to investigating the interfacial reinforcing capabilities of the LIG, the ability of the LIG to detect delamination between LIG interfaces was also simultaneously evaluated during Mode I interlaminar fracture toughness testing. The applied load and change in resistance with increasing crosshead extension of a representative Mode I sample is shown in Fig. 9A. It is immediately clear from the figure that there is a strong correlation between the load and change in resistance with crosshead extension. As the extension increases and the double cantilever beam sample is delaminated, the crack length is found to increase, while the load required to pull apart the specimen and propagate the crack is decreased. As the decreasing trend in the load is observed, the rate of change in the double cantilever beams resistance increases, thus showing a correlation between delamination and electrical impedance. When the extension reaches 22 mm, the load decreases dramatically,

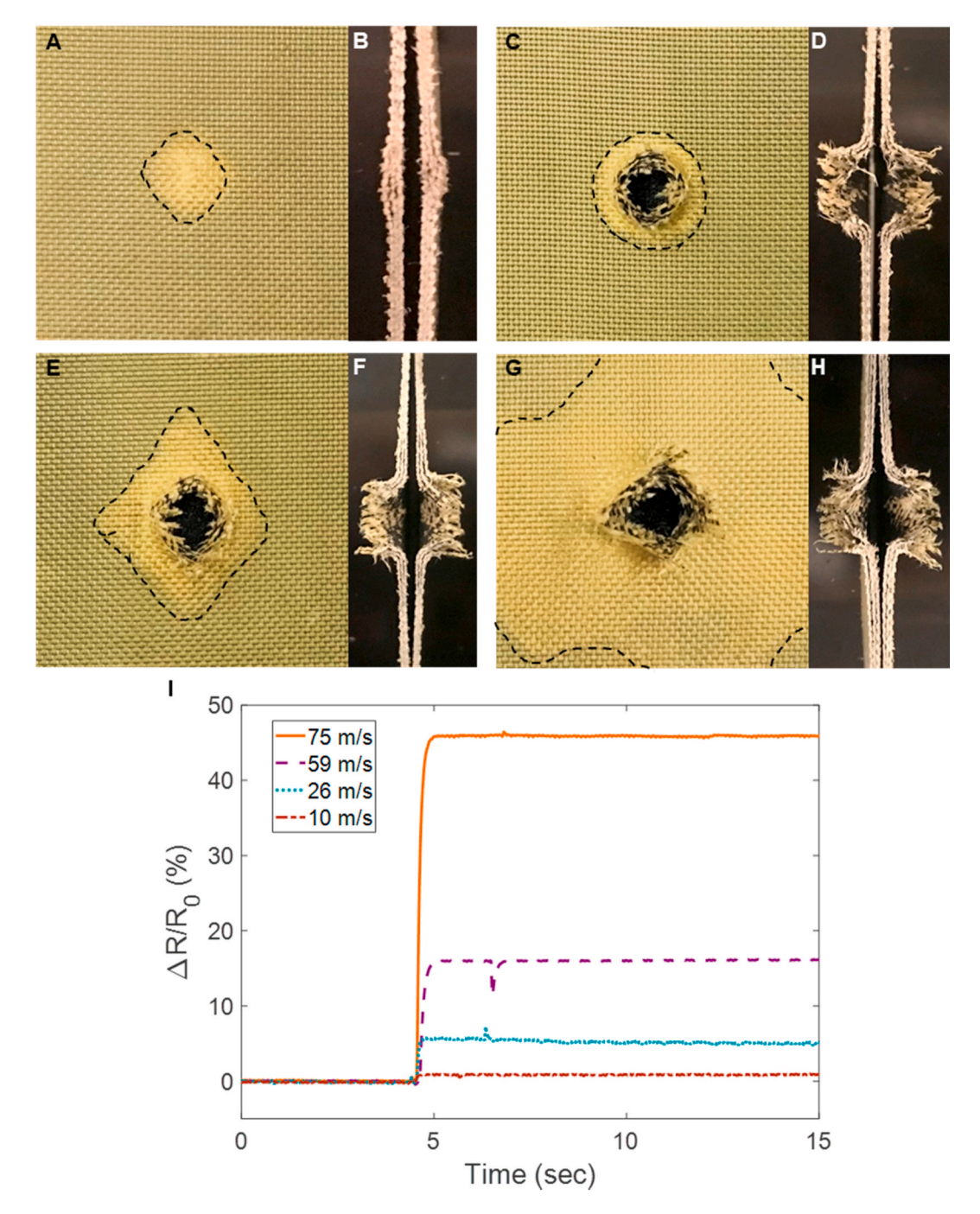


Fig. 6. Images of impacted laminates with increased delamination between the composite plies imaged from the top surface at speeds of A) 10 m/s, C) 26 m/s, E) 59 m/s, G) 75 m/s and cross-section images at speeds of B) 10 m/s, D) 26 m/s, F) 59 m/s, H) 75 m/s. I) Corresponding percent change in impedance for each sample.

indicating rapid crack propagation within the interlaminar region, which is accompanied by a significant increase in specimen impedance, resulting in a confirmed direct correlation between crack growth and change in impedance. It is thus apparent that the piezoresistive LIG not only detects delamination, but can also provide insight into the rate at which the delamination grows. For additional analysis, the relationship between the change in the resistance of the double cantilever beam and the crack length is shown in Fig. 9B. Overall, the percent change in resistance increases with increasing crack length, which correlates to increasing inter-ply delamination. As the crack propagates through the interlaminar region, the conductive contacts between the LIG surfaces are decreased, therefore restricting current pathways causing a measured increase in impedance. Thus, the LIG exhibits

multifunctionality in both reinforcing the interface between plies while also enabling structural health monitoring of this failure-prone area within fiber-reinforced composites.

4. Conclusion

A method for in-situ impact and delamination damage detection for aramid fiber reinforced composites is presented here using an integrated piezoresistive LIG interleave. The addition of the LIG does not add extra weight or interlaminar thickness to the sample and does not require external bonding since the LIG is generated using the aramid fibers as a precursor. Furthermore, the LIG process does not require extreme processing conditions and can be completed at room temperature and

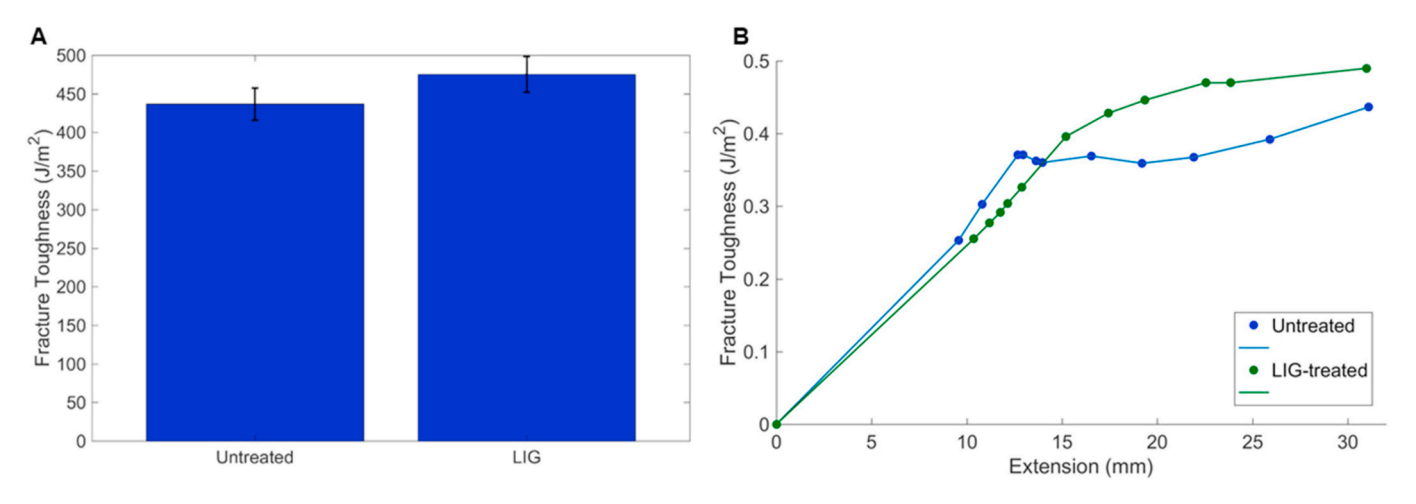


Fig. 7. Mode I interlaminar fracture toughness of untreated aramid composite and LIG-treated aramid composite. B) Average fracture toughness. B) Representative fracture toughness vs extension plots.

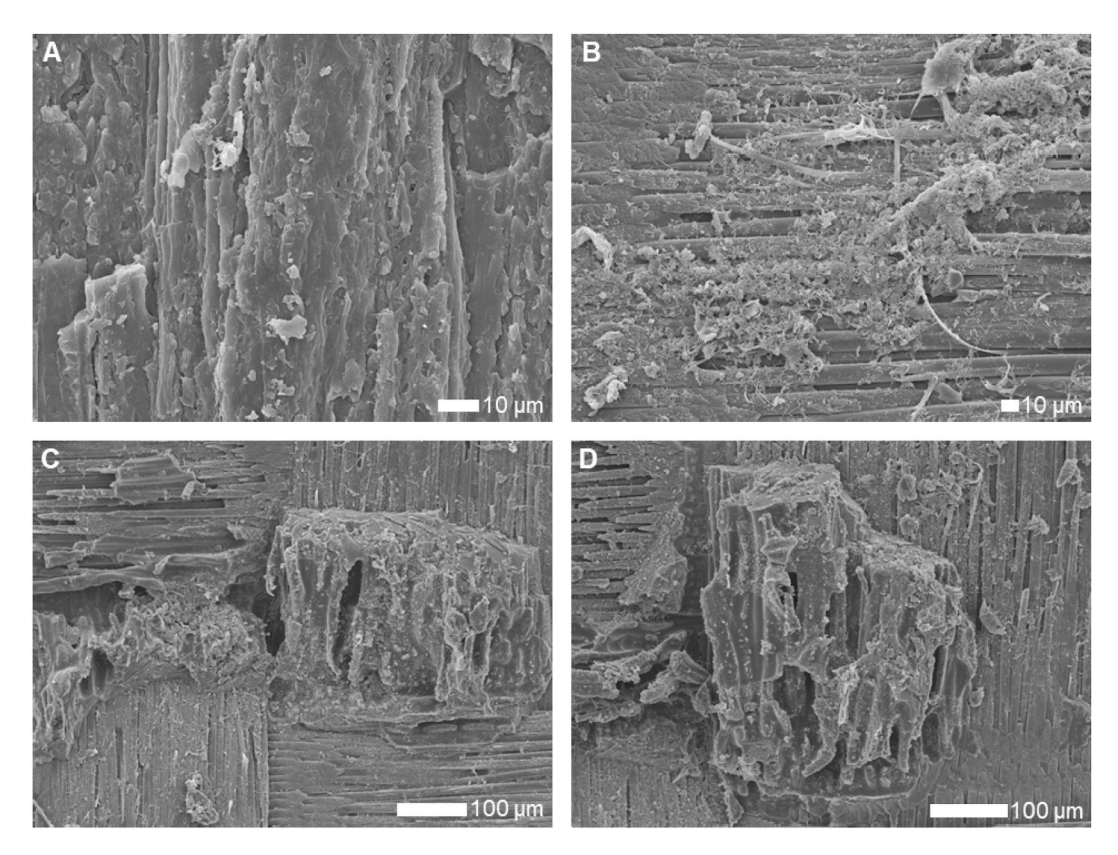


Fig. 8. A, B, C, D) Mode I interlaminar fracture toughness fracture surfaces of LIG-treated aramid fiber reinforced composite.

atmospheric pressure using a commercial CO_2 laser printer which contributes to the scalability of the method. The LIG-treated aramid fiber reinforced composites were successfully shown to detect ballistic damage in-situ using a four-point probe resistance monitoring method and the percent change in electrical impedance was found to directly correlate to the projectile impact velocity. Therefore, a prediction of failure, damage extent, and projectile impact velocity can be made through correlation of impedance change and projectile velocity. Mode I interlaminar fracture toughness testing also evaluated the relation between change in resistance and generated delamination; a common form of damage experienced by ballistic composites. Furthermore, the addition of LIG within the aramid composite was shown to improve both the areal-density-specific V_{50} and the Mode I interlaminar fracture

toughness. Thus, the results of this work demonstrate the multifunctionality of LIG-treated aramid composites and shows that the LIG piezoresistivity can be exploited to predict impact velocity and delamination extent, providing an estimate of the scope of damage sustained by the composites during ballistic impact.

CRediT authorship contribution statement

Kelsey Steinke: Conceptualization, Investigation, Writing - original draft. LoriAnne Groo: Conceptualization, Investigation, Writing - review & editing. Henry A. Sodano: Conceptualization, Project administration, Methodology, Funding acquisition, Supervision, Writing - review & editing.

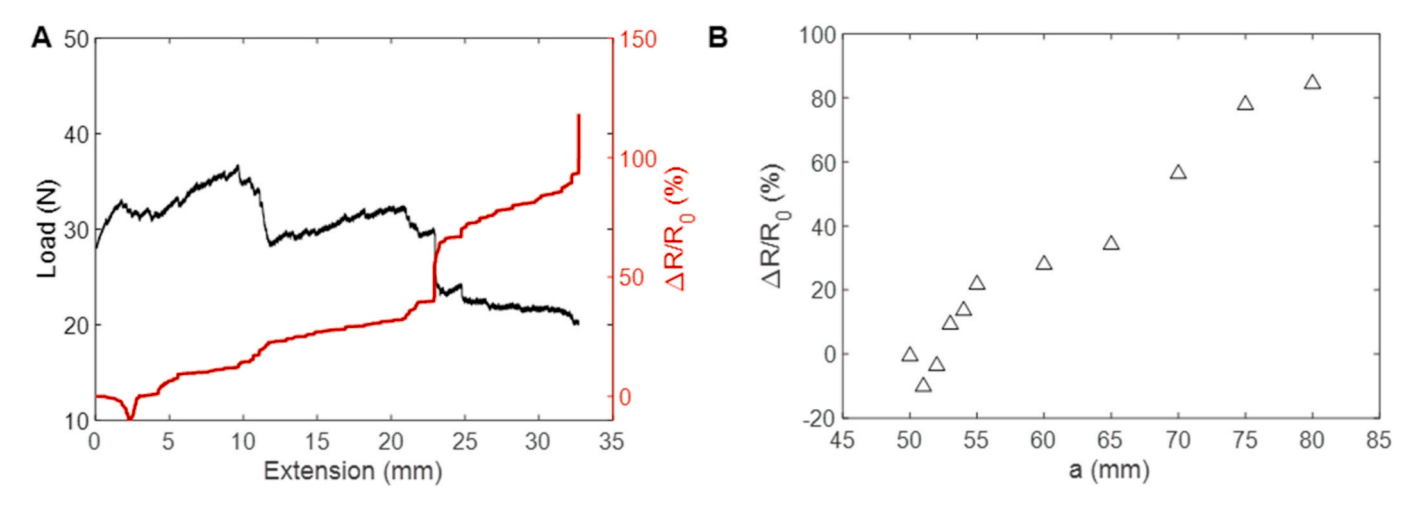


Fig. 9. A) Applied load and percent change in resistance versus extension during Mode I interlaminar fracture toughness test. B) Percent change in resistance versus crack length during Mode I interlaminar fracture toughness test.

Declaration of competing interest

The authors declare that they have no known competing financial interests or personal relationships that could have appeared to influence the work reported in this paper.

Acknowledgments

The authors gratefully acknowledge financial support for this research from the National Science Foundation Graduate Research Fellowship Program, the National Science Foundation under grant # CMMI-1762369, and the Army Research Office under grant #W911NF-18-1-0061.

References

- [1] T.J. Singh, S. Samanta, Characterization of kevlar fiber and its composites: a review, in: Mater. Today Proc, Elsevier Ltd, 2015, pp. 1381–1387, https://doi.org/
- [2] V.P. McConnell, Ballistic protection materials a moving target, Reinforc Plast 50 (2006) 20–25. https://doi.org/10.1016/S0034-3617(06)71187-0.
- [3] D. Rosato, Reinforced Plastics Handbook Donald V Rosato, Dominick V Rosato Google Books, 2004. https://books.google.com/books?hl=en&lr=&id=g7R 8g-l_KO8C&oi=fnd&pg=PP1&dq=18.+Rosato+DV,+Rosato+DV+.
- [4] K. Imielińska, M. Castaings, R. Wojtyra, J. Haras, E. Le Clezio, B. Hosten, Air-coupled ultrasonic C-scan technique in impact response testing of carbon fibre and hybrid: glass, carbon and Kevlar/epoxy composites, J. Mater. Process. Technol. (2004) 513–522, https://doi.org/10.1016/j.jmatprotec.2004.07.143.
- [5] S. Fidan, T. Sınmazcelik, E. Avcu, M. Ozgur Bora, O. Coban, Detecting Impact Damages in an Aramid/Glass Fiber Reinforced Hybrid Composite with Micro Tomography, 2012. https://doi.org/10.4028/www.scientific.net/AMR.445.9.
- [6] J. Parthenios, D.G. Katerelos, G.C. Psarras, C. Galiotis, Aramid fibers; a multifunctional sensor for monitoring stress/strain fields and damage development in composite materials, Eng. Fract. Mech. 69 (2002) 1067–1087, https://doi.org/ 10.1016/S0013-7944(01)00123-0.
- [7] I. Zivkovic, A. Kojovic, R. Aleksic, I. Živković, K. Maksimović, A. Kojović, R. Aleksić, Analysis of Smart Aramid Fiber Reinforced Laminar Thermoplastic Composite Material under Static Loading, 2008. https://www.researchgate.net/publication/265892293. (Accessed 2 February 2020).
- [8] D.I. Rosa M, Damage Mechanisms in Loaded Aramid Composites by Means of Embedded PVDF Acoustic Emission Sensors, 2006. https://doi.org/10.4028/www. scientific.net/AMR.13-14.337.
- [9] L. Groo, D.J. Inman, H.A. Sodano, In situ damage detection for fiber-reinforced composites using integrated zinc oxide nanowires, Adv. Funct. Mater. 28 (2018) 1802846. https://doi.org/10.1002/adfm.201802846.
- [10] G. Kister, B. Ralph, G.F. Fernando, Damage Detection in Glass Fibre-Reinforced Plastic Composites Using Self-Sensing E-Glass Fibres, 2004, https://doi.org/ 10.1088/0964-1726/13/5/021
- K.S.C. Kuang, W.J. Cantwell, Use of conventional optical fibers and fiber Bragg gratings for damage detection in advanced composite structures: a review, Appl. Mech. Rev. 56 (2003) 493–513, https://doi.org/10.1115/1.1582883.
 S. Huguet, N. Godin, R. Gaertner, L. Salmon, D. Villard, Use of acoustic emission to
- [12] S. Huguet, N. Godin, R. Gaertner, L. Salmon, D. Villard, Use of acoustic emission to identify damage modes in glass fibre reinforced polyester, Compos. Sci. Technol. 62 (2002) 1433–1444, https://doi.org/10.1016/S0266-3538(02)00087-8.

- [13] S. Barré, M.L. Benzeggagh, On the use of acoustic emission to investigate damage mechanisms in glass-fibre-reinforced polypropylene, Compos. Sci. Technol. 52 (1994) 369–376. https://doi.org/10.1016/0266-3538(94)90171-6.
- [14] L. Böger, M.H.G. Wichmann, L.O. Meyer, K. Schulte, Load and health monitoring in glass fibre reinforced composites with an electrically conductive nanocomposite epoxy matrix, Compos. Sci. Technol. 68 (2008) 1886–1894, https://doi.org/ 10.1016/j.compscitech.2008.01.001.
- [15] S. Gao, R.-C. Zhuang, J. Zhang, J.-W. Liu, E. M\u00e4der, Glass fibers with carbon nanotube networks as multifunctional sensors, Adv. Funct. Mater. 20 (2010) 1885–1893, https://doi.org/10.1002/adfm.201000283.
- [16] I. Weber, P. Schwartz, Monitoring bending fatigue in carbon-fibre/epoxy composite strands: a comparison between mechanical and resistance techniques, Compos. Sci. Technol. 61 (2001) 849–853, https://doi.org/10.1016/S0266-3538 (01)00028-8.
- [17] M. Kupke, K. Schulte, R. Schüler, Non-destructive testing of FRP by d.c. and a.c. electrical methods, Compos. Sci. Technol. 61 (2001) 837–847, https://doi.org/10.1016/S0266-3538(00)00180-9.
- [18] J.C. Abry, S. Bochard, A. Chateauminois, M. Salvia, G. Giraud, In situ detection of damage in CFRP laminates by electrical resistance measurements, Compos. Sci. Technol. 59 (1999) 925–935, https://doi.org/10.1016/S0266-3538(98)00132-8.
- [19] K. Schulte, C. Baron, Load and failure analyses of CFRP laminates by means of electrical resistivity measurements, Compos. Sci. Technol. 36 (1989) 63–76, https://doi.org/10.1016/0266-3538(89)90016-X.
- [20] M. Sánchez, R. Moriche, S.G. Prolongo, A.R. Marrón, A. Jiménez-Suárez, A. Ureña, Evaluation of sensitivity for detecting different failure modes of epoxy matrix composites doped with graphene nanoparticles, Compos. Struct. 225 (2019), https://doi.org/10.1016/j.compstruct.2019.111167.
- [21] X. Du, H. Zhou, W. Sun, H.Y. Liu, G. Zhou, H. Zhou, Y.W. Mai, Graphene/epoxy interleaves for delamination toughening and monitoring of crack damage in carbon fibre/epoxy composite laminates, Compos. Sci. Technol. 140 (2017) 123–133, https://doi.org/10.1016/j.compscitech.2016.12.028.
- [22] M. Nofar, S.V. Hoa, M.D. Pugh, Failure detection and monitoring in polymer matrix composites subjected to static and dynamic loads using carbon nanotube networks, Compos. Sci. Technol. 69 (2009) 1599–1606, https://doi.org/10.1016/j. compositech. 2009.03.010.
- [23] N.D. Alexopoulos, C. Bartholome, P. Poulin, Z. Marioli-Riga, Structural health monitoring of glass fiber reinforced composites using embedded carbon nanotube (CNT) fibers, Compos. Sci. Technol. 70 (2010) 260–271, https://doi.org/10.1016/ j.compscitech.2009.10.017.
- [24] L. Gao, E.T. Thostenson, Z. Zhang, T.-W. Chou, Sensing of damage mechanisms in fiber-reinforced composites under cyclic loading using carbon nanotubes, Adv. Funct. Mater. 19 (2009) 123–130, https://doi.org/10.1002/adfm.200800865.
- [25] D.J. Kwon, Z.J. Wang, J.Y. Choi, P.S. Shin, K.L. Devries, J.M. Park, Damage sensing and fracture detection of CNT paste using electrical resistance measurements, Compos. B Eng. 90 (2016) 386–391, https://doi.org/10.1016/j.
- [26] M. Tehrani, A.Y. Boroujeni, T.B. Hartman, T.P. Haugh, S.W. Case, M.S. Al-Haik, Mechanical characterization and impact damage assessment of a woven carbon fiber reinforced carbon nanotube-epoxy composite, Compos. Sci. Technol. 75 (2013) 42–48, https://doi.org/10.1016/j.compscitech.2012.12.005.
- [27] F.H. Gojny, M.H.G. Wichmann, U. Köpke, B. Fiedler, K. Schulte, Carbon nanotube-reinforced epoxy-composites: enhanced stiffness and fracture toughness at low nanotube content, Compos. Sci. Technol. 64 (2004) 2363–2371, https://doi.org/10.1016/j.compscitech.2004.04.002
- [28] J. Lin, Z. Peng, Y. Liu, F. Ruiz-Zepeda, R. Ye, E.L.G. Samuel, M.J. Yacaman, B. I. Yakobson, J.M. Tour, Laser-induced porous graphene films from commercial polymers, Nat. Commun. 5 (2014), https://doi.org/10.1038/ncomms6714.

- [29] D.X. Luong, K. Yang, J. Yoon, S.P. Singh, T. Wang, C.J. Arnusch, J.M. Tour, Laser-induced graphene composites as multifunctional surfaces, ACS Nano (2019), acsnano.8b09626, https://doi.org/10.1021/acsnano.8b09626.
- [30] Y. Chyan, R. Ye, Y. Li, S.P. Singh, C.J. Arnusch, J.M. Tour, Laser-induced graphene by multiple lasing: toward electronics on cloth, paper, and food, ACS Nano 12 (2018) 2176–2183, https://doi.org/10.1021/acsnano.7b08539.
- [31] L.Q. Tao, H. Tian, Y. Liu, Z.Y. Ju, Y. Pang, Y.Q. Chen, D.Y. Wang, X.G. Tian, J. C. Yan, N.Q. Deng, Y. Yang, T.L. Ren, An intelligent artificial throat with sound-sensing ability based on laser induced graphene, Nat. Commun. 8 (2017), https://doi.org/10.1038/ncomms14579.
- [32] L.X. Duy, Z. Peng, Y. Li, J. Zhang, Y. Ji, J.M. Tour, Laser-induced graphene fibers, Carbon N. Y. 126 (2018) 472–479, https://doi.org/10.1016/j.carbon.2017.10.036.
- [33] R. Rahimi, M. Ochoa, W. Yu, B. Ziaie, Highly stretchable and sensitive unidirectional strain sensor via laser carbonization, ACS Appl. Mater. Interfaces 7 (2015) 4463–4470, https://doi.org/10.1021/am509087u.
- [34] Y. Wang, Y. Wang, P. Zhang, F. Liu, S. Luo, Laser-induced freestanding graphene papers: a new route of scalable fabrication with tunable morphologies and properties for multifunctional devices and structures, Small 14 (2018), 1802350, https://doi.org/10.1002/smll.201802350.

- [35] S. Luo, P.T. Hoang, T. Liu, Direct laser writing for creating porous graphitic structures and their use for flexible and highly sensitive sensor and sensor arrays, Carbon N. Y. 96 (2016) 522–531, https://doi.org/10.1016/j.carbon.2015.09.076.
- [36] L.A. Groo, J. Nasser, D.J. Inman, H.A. Sodano, Laser induced graphene for in situ damage sensing in aramid fiber reinforced composites, Compos. Sci. Technol. 201 (2020) 108541.
- [37] J. Nasser, L.A. Groo, L. Zhang, H. Sodano, Laser induced graphene fibers for multifunctional aramid fiber reinforced composite, Carbon N. Y. 158 (2020) 146–156, https://doi.org/10.1016/j.carbon.2019.11.078.
- [38] J.S. Stenzler, N. Goulbourne, D. Dillard, A. Wicks, T. Long, Impact Mechanics of PMMA/PC Multi-Laminates with Soft Polymer Interlayers, 2009.
- [39] E.J. Garcia, B.L. Wardle, A. John Hart, Joining prepreg composite interfaces with aligned carbon nanotubes, Compos. Part A Appl. Sci. Manuf. 39 (2008) 1065–1070, https://doi.org/10.1016/j.compositesa.2008.03.011.
- [40] J. Joaquí, J. Blanco, E.J. García, G. Garcíía, R. Guzmánguzmaá, G. De Villoria, B.L. Wardle, Limiting mechanisms of mode I interlaminar toughening of composites reinforced with aligned carbon nanotubes, (n.d.). https://doi.org/10.1177/0021998309102398.